Research Square

Preprints are preliminary reports that have not undergone peer review.
They should not be considered conclusive, used to inform clinical practice,
or referenced by the media as validated information.

Construction of 0D/2D M/rGO@EuMOF Multiscale Heterostructures for Integrated High-Efficiency Microwave Absorption and Corrosion Protection

Xingke Ye
A VIC Chengdu Aircraft Industrial (Group) Co., Ltd
Ning Yan
A VIC Chengdu Aircraft Industrial (Group) Co., Ltd
Huimei Fuyao
A VIC Chengdu Aircraft Industrial (Group) Co., Ltd
Qi Deng
A VIC Chengdu Aircraft Industrial (Group) Co., Ltd
Congcong Sun
A VIC Chengdu Aircraft Industrial (Group) Co., Ltd
Renchi Qin
Southwest Jiaotong University
Shihan Ma
Southwest Jiaotong University
Yuxing Li
Southwest Jiaotong University
Zhuheng Yao
Southwest Jiaotong University
Qing Qi
qi_qing7@163.com

Southwest Jiaotong University
Fanbin Meng
Southwest Jiaotong University

Research Article

Keywords: MBene, EuMOF, 0D-2D heterostructure, Microwave absorption, Corrosion protection, Impedance matching

Posted Date: September 14th, 2026

DOI: https://doi.org/10.21203/rs.3.rs-10862546/v1

License: This work is licensed under a Creative Commons Attribution 4.0 International License.
Read Full License

Additional Declarations: No competing interests reported.

Construction of 0D/2D M/rGO@EuMOF Multiscale Heterostructures for Integrated High-Efficiency Microwave Absorption and Corrosion Protection

Xingke Ye[a], Ning Yan[a], Huimei Fuyao[a], Qi Deng[a], Congcong Sun[a], Renchi Qin[b], Shihan Ma[b], Yuxing Li[b], Zhuheng Yao[b], Qing Qi[b]*, Fanbin Meng[b]*

a AVIC Chengdu Aircraft Industrial (Group) Co., Ltd., Chengdu 610092, China

b Key Laboratory of Advanced Technologies of Materials (Ministry of Education), School of Materials Science and Engineering, Southwest Jiaotong University, Chengdu, 610031, China

Email: qi_qing7@163.com, mengfanbin_wing@126.com

Keywords: MBene, EuMOF, 0D-2D heterostructure, Microwave absorption, Corrosion protection, Impedance matching

Abstract

Developing multifunctional materials with simultaneous microwave absorption and corrosion resistance is of great significance for practical applications in complex marine environments. Herein, a series of multiscale zero-dimensional/two-dimensional(0D/2D) heterostructure composites, denoted as M/rGO@EuMOF (MG@E), were successfully fabricated through a facile in-situ hydrothermal strategy. In this design, zero-dimensional europium-based metal-organic framework (EuMOF) microspheres were uniformly anchored onto two-dimensional M/rGO nanosheets, enabling optimized impedance matching and enhanced electromagnetic attenuation. Structural characterizations demonstrate the successful coordination and homogeneous distribution of EuMOF particles on the M/rGO surface, forming stable heterogeneous interfaces while preserving the conductive and magnetic framework of the substrate. Benefiting from the synergistic effects of interfacial polarization at the 0D/2D heterointerfaces, dipole polarization induced by MOF ligands, conductive loss, and magnetic dissipation, the MG@E composites exhibit remarkable microwave absorption performance. In particular, the MG@E3 sample achieves an optimal reflection loss (RLmin) of −54.02 dB at a thickness of 2.1 mm and a maximum effective absorption bandwidth (EAB) of 4.5 GHz at only 1.4 mm. Meanwhile, electrochemical measurements confirm that the MG@E coatings possess robust anti-corrosion properties toward Q235 steel, where the MG@E2 sample maintains a corrosion protection efficiency of 94.8% after 21 days of immersion in 3.5wt.% NaCl solution. This enhanced corrosion resistance is attributed to the synergistic barrier effect generated by the filling of 0D microspheres within the 2D labyrinth structure. This work provides a feasible strategy for the rational design of integrated microwave absorbing materials with superior environmental adaptability and long-term service reliability.

1. Introduction

Driven by the rapid advancement of radar detection and wireless communication technologies, electromagnetic wave (EMW) absorbing materials have attracted increasing attention for applications in military stealth and

electromagnetic interference mitigation [1-4]. Despite remarkable progress in electromagnetic attenuation performance, most reported microwave absorbers still suffer from inadequate environmental durability, particularly under aggressive marine conditions characterized by high humidity and chloride-rich electrolytes [5-7]. The continuous ingress of corrosive media not only accelerates coating degradation and substrate corrosion but also disrupts the electromagnetic attenuation network, resulting in a rapid deterioration of microwave absorption performance [8, 9]. Therefore, simultaneously achieving efficient electromagnetic attenuation and long-term corrosion protection remains a fundamental challenge for multifunctional protective coatings. Developing integrated material systems capable of balancing these two functions is of considerable scientific significance and practical importance for advanced marine and defense applications [10, 11].

As an emerging family of layered two-dimensional materials, MBenes exhibit great prospects for EMW absorption owing to large specific surface area, metallic conductivity and inherent ferromagnetism [12, 13]. MBenes (such as Fe_2AlB_2) not only possess high conductivity, enabling the construction of continuous three-dimensional conductive networks within the matrix and inducing strong multiple interfacial polarizations for efficient dielectric loss, but their intrinsic ferromagnetism also endows the material with magnetic loss capabilities. This dual-loss nature effectively addresses the impedance mismatch issues often found in materials with a single electromagnetic loss mechanism. Furthermore, from a corrosion protection perspective, 2D lamellar materials can be layered within a polymer matrix to construct a "maze effect." This significantly extends the diffusion path for corrosive media (such as Cl^- and H_2O) to reach the metal substrate, thereby granting the coating exceptional physical barrier properties [14]. Research indicates that by modifying the surface of 2D nanosheets or compounding them with materials of other dimensions, interfacial compatibility can be further enhanced, reducing micro-pore defects in the coating and achieving long-term anti-corrosion [15-21].

To further optimize impedance matching and introduce more polarization centers, the construction of multi-dimensional heterostructures has become a research hotspot in recent years [22]. Reduced graphene oxide (rGO), as a typical 2D conductive material, can significantly improve the conduction loss of the system due to its extremely high carrier mobility [23, 24]. However, excessive conductivity often leads to strong electromagnetic reflection rather than absorption. Therefore, the introduction of metal-organic frameworks (MOFs) with unique porous structures and abundant functional groups has become key to regulating the complex permittivity [25-27]. MOF materials can induce dipole polarization through their unique framework structures and generate substantial charge accumulation at 0D/2D hetero-interfaces, enhancing interfacial polarization loss [28, 29]. Additionally, MOF materials have shown unique advantages in the anti-corrosion field; their porous structures can serve as carriers for corrosion inhibitors or improve coating density through physical filling effects [30-32].

In this contribution, aiming to satisfy dual requirements of high-efficiency microwave attenuation and long-term anti-corrosion in aggressive marine environments, 0D Eu-based MOF microspheres are in-situ anchored onto prefabricated 2D M/rGO via one-pot hydrothermal reaction to construct novel 0D/2D MG@E heterostructured composites. Systematic characterizations are implemented to reveal the loading-dependent evolution of microstructure, electromagnetic loss mechanism and anti-corrosion performance. The synergistic optimization of impedance matching and multi-loss mechanisms endows MG@E composites with dual-functional superiority, offering a facile route to

develop environment-adaptive multifunctional protective coatings. Unlike conventional MOF-derived absorbers that rely on pyrolysis to generate conductive carbon frameworks, the present work directly utilizes EuMOF as an intact dielectric modulation component, enabling simultaneous optimization of impedance matching and corrosion barrier properties without sacrificing the intrinsic conductivity and magnetic response of MBene.

2. Experimental

2.1 Materials

Fe_2AlB_2 powder with a particle size of 400 mesh was purchased from Jilin Yiyi Technology Co., Ltd. Sodium hydroxide (analytical grade), hydrochloric acid (analytical grade), paraffin wax (pathological grade) and anhydrous ethanol (analytical grade) were supplied by Shanghai Macklin Biochemical Technology Co., Ltd. and Shanghai Aladdin Biochemical Technology Co., Ltd., respectively. Super P Li conductive carbon black was obtained from Zhuguang New Energy Materials Technology Company. Polyvinylidene fluoride (PVDF, molecular weight = 700,000, purity ≥99%) was purchased from Zhongxin Plastic Co., Ltd. Liquid epoxy resin and its matching No.650 curing agent were provided by Chengdu Sanhong High-tech Technology Co., Ltd. Sodium chloride (analytical grade) was sourced from Chengdu Haihong Experimental Instrument Co., Ltd. Q235 carbon steel of industrial grade was obtained from Chengdu Kelong Chemical Reagent Factory. Deionized water used throughout the experiments was self-prepared in the laboratory.

2.2 Preparation of the Fe_2AlB_2 working electrode in the MAB phase

0.1 g pristine Fe_2AlB_2 powder was immersed into 50 mL 1 M HCl solution and mildly stirred for 30 s to remove surface native alumina layer. After triple rinsing with deionized water, the obtained solid was vacuum-dried at 40 °C for 12 h. The dried Fe_2AlB_2 powder was blended with 0.03 g Super P Li carbon black and 0.015 g PVDF, with appropriate N-methylpyrrolidone (NMP) added as solvent. After 10 min grinding, the homogeneous slurry was uniformly coated onto nickel foam (1 cm × 1.2 cm × 0.5 mm), followed by oven drying at 50 °C for 6 h to obtain working electrodes.

2.3 Electrochemical etching of the MAB phase of Fe_2AlB_2

A Fe_2AlB_2-coated foam nickel electrode was used as the working electrode, a platinum foil as the counter electrode, and a silver chloride electrode (Ag/AgCl) as the reference electrode to form a three-electrode system. The electrolytic cell was heated to 70 °C and a constant current density of $0.5 mA \cdot cm^{-2}$ was applied to selectively strip Al atoms from MAB phase in 20 wt.% NaOH electrolyte via the reaction:

$$Al + 4OH^- \rightarrow [Al(OH)_4]^- + 3e^-$$

Following electrochemical etching, the foam nickel mesh was placed in an NMP solution and sonicated for 30 min; the etched particles were then separated using magnetic separation, whilst being washed repeatedly with NMP and deionised water. Finally, the sample was freeze-dried for 24 h to yield the etched iron-based MBene-phase $Fe_2Al_{(1-x)}B_2$.

2.4 Preparation of MBene/rGO composites

0.5g of MBene was added to 150 mL of an ethanol/water mixture (volume ratio 9:1), together with 4 mL of glacial acetic acid, and stirred for 30 min. Subsequently, 1 g of 3-aminopropyltrimethoxysilane (APTES) was added, and the mixture was stirred at room temperature for 24 h. The resulting material was then collected via magnetic separation and freeze-dried to yield amino-modified, cationic MBene. Disperse 0.3 g of the modified MBene in 50 mL of deionised water, simultaneously adding GO at a mass fraction of 2 wt% relative to MBene. Treat with ultrasound for 30 min, stir for 2 h, and allow MBene and GO to form a composite via the attraction of positive and negative surface charges. Subsequently, collect the composite via magnetic separation, wash repeatedly with deionised water, and dried under vacuum at 60 °C for 12 h to obtain the MBene/GO composite. The MBene/GO composite was dispersed in 50mL of deionised water, and sodium ascorbate was added to chemically reduce the MBene/GO, with a mass ratio of sodium ascorbate to GO of 1:1. The reduction was carried out at 50 °C for 2 h. The reduced MBene/rGO was separated magnetically, washed alternately with anhydrous ethanol and deionised water, and then dried to yield the final M/rGO composite system.

2.5 Preparation of EuMOF

Add 0.2 mmol of europium nitrate hexahydrate to 16 mL of deionised water and sonicate for 20 min to ensure uniform dispersion. Disperse an amount of BTDA equivalent in moles to the europium nitrate hexahydrate in 12 mL of DMF, stir for 20 min, and then add this solution to the mixture. To ensure the homogeneity of the mixture, the beaker containing the reactants was subjected to ultrasonication for 20 min, followed by a total of five freeze-vacuum-thaw degassing cycles. The reaction mixture was transferred to a 50 mL PTFE-lined stainless steel reactor and maintained at 125 °C for 20 h. After the system had cooled naturally to room temperature, it was centrifuged at 8000 rpm for 5 min, and the product was washed four times with anhydrous ethanol and four times with deionised water, respectively. The washed solid was freeze-dried for 48 h to yield the target product, the EuMOF composite material.

2.6 Preparation of M/rGO@EuMOF

Dissolve 0.3 g of MBene/rGO in 16 mL of deionised water, whilst simultaneously adding 0.05 mmol, 0.1 mmol, 0.15 mmol and 0.2 mmol of europium nitrate hexahydrate, and sonicate for 20 min to ensure uniform dispersion. Disperse an amount of BTDA equivalent in moles to the europium nitrate hexahydrate in 12 mL of DMF, stir for 20 min, and then add this solution to the mixture. To ensure the homogeneity of the solution mixture, the beaker containing the reactants was subjected to ultrasonication for 20 min, followed by a total of five freeze-vacuum-thaw degassing cycles. The reaction mixture was transferred to a 50 mL PTFE-lined stainless steel reactor and maintained at 125 °C for 20 h. After the system had cooled naturally to room temperature, the product was collected via magnetic separation and washed four times each with anhydrous ethanol and deionised water, before being freeze-dried for 48 h to yield M/rGO@EuMOF. Depending on the EuMOF concentration, the products were named MG@E1, MG@E2, MG@E3 and MG@E4 respectively.

2.7 Preparation of the M/rGO@EuMOF epoxy resin composite coating

Weigh out 0.02 g of M/rGO@EuMOF powder, place it in 2 mL of ethanol, and sonicate for 15 min. Once uniformly dispersed, add 1.42 g of epoxy resin and mix for 10 minutes using a mechanical stirrer to ensure thorough dispersion. Subsequently, 1.42 g of curing agent was added, and stirring was continued for 20 min. The resulting homogeneous mixture was degassed under vacuum, then applied to the surface of Q235 steel and air-dried at room

temperature for 48 h. The coatings were similarly designated as MG@E1, MG@E2, MG@E3 and MG@E4.

2.8 Characterization

The microstructures of Fe_2AlB_2 and $Fe_2A_{(1-x)}B_2$ were characterised using a scanning electron microscope (SEM, JEOL JSM-7800F), and their surface elemental composition and distribution were analysed using an energy-dispersive spectrometer (EDS). A transmission electron microscope (TEM, JEOL Jem F200) was used to further examine the microstructures of Fe_2AlB_2 and $Fe_2A_{(1-x)}B_2$. A Cu-Kα X-ray diffractometer (XRD, PW1830, Philips) was used to characterise the structure of Fe_2AlB_2 and $Fe_2A_{(1-x)}B_2$ and analyse their crystallisation behaviour, with a scanning speed of 5°/min and a scanning range of 10°–90°. Using a monochromatic Al-Kα X-ray source (1486.6 eV), the chemical composition and bonding types of Fe_2AlB_2 and $Fe_2A_{(1-x)}B_2$ were investigated via X-ray photoelectron spectroscopy (XPS, Thermo Scientific K-Alpha). Fe_2AlB_2 and $Fe_2A_{(1-x)}B_2$ were uniformly mixed with paraffin wax, and moulds were used to press the mixture into annular test samples with an outer diameter of 7.0 mm and an inner diameter of 3.04 mm, with a material mass ratio of 80%. Their electromagnetic parameters were measured in the frequency range of 1.0–18.0 GHz using a vector network analyser (3671D). Using the Shanghai Chenhua electrochemical workstation (CHI760E), EIS and potential-current polarisation (PDP) tests were performed on the prepared working electrode in three-electrode mode, comprising the working electrode (Q235 steel coated with the coating, contact area 1cm^2), the reference electrode (saturated silver chloride electrode) and the counter electrode (platinum foil, area 4 cm^2). The EIS tests were conducted within a frequency range of 10^{-2}-10^5Hz, with an AC signal amplitude of 10mV. RCS simulations of the coating were performed using CST Microwave Studio software at a simulation frequency of 6.015 GHz, with a thickness set at 2.3 mm. Furthermore, MBene and MBene/rGO were uniformly mixed with paraffin wax, and a mould was used to press the mixture into ring-shaped test specimens with an outer diameter of 7.0 mm and an inner diameter of 3.04 mm, with a mass ratio of 75%. Their electromagnetic parameters were measured using a vector network analyser (3671D) within the frequency range of 1.0-18.0GHz.

3. Results and Discussion

3.1 Morphological characterisation of M/rGO@EuMOF

Schematic diagram of the preparation process for M/rGO@EuMOF was shown in Fig.1a. The SEM images clearly illustrate the evolution of the microstructure of EuMOF and the composite material formed by combining it with M/rGO. Fig. 1b–c show the pure EuMOF sample, in which a large number of particles are evenly distributed across the substrate surface with good dispersion; no extensive agglomeration is observed, indicating that nucleation of EuMOF was relatively uniform during the preparation process. Upon further magnification, it can be observed that these particles primarily exhibit a regular spherical or sub-spherical morphology, with distinct edges and relatively smooth surfaces. The particle size is on the micrometre scale; whilst there is slight contact between some of the microspheres, the overall dispersion remains good. Upon composite formation between EuMOF and M/rGO, the material morphology undergoes a marked change. As shown in Fig. 1d–e, the EuMOF no longer exhibits a spherical shape but instead forms larger, irregular block-like structures, with the main body displaying wrinkled and stacked features, indicating that the two-dimensional M/rGO sheets act as a scaffold in the composite process; simultaneously, minute spherical particles adhering to the surface can still be clearly observed in local regions, indicating that the EuMOF has been successfully anchored to the M/rGO surface. At this stage, the EuMOF loading is relatively low,

and the contour of the M/rGO layers remains distinct, with no continuous coating yet formed. As the EuMOF content is further increased, the volume of the composite particles increases and the surface is gradually filled with EuMOF particles; the originally distinct pleated layered structure begins to blur. In Fig. 1e, numerous regions of particle accumulation appear on the material surface, indicating that the nucleation and growth of EuMOF on the M/rGO surface have become more thorough; the particles begin to interconnect and overlap, resulting in a tighter interfacial bond. By Fig. 1f, the overall surface of the composite particles tends towards a continuous, smooth surface, and the original two-dimensional layered characteristics of the M/rGO are significantly diminished, indicating that EuMOF has achieved extensive encapsulation and growth. This morphological change suggests that the interaction between EuMOF and M/rGO is not merely a simple physical mixture, but rather the formation of a relatively stable heterogeneous composite interface. Under the highest loading conditions, the particle surface is largely covered by EuMOF particles, presenting an overall denser, block-like morphology with distinct spherical protrusions visible on the surface. Although the increased EuMOF loading leads to greater coverage, no significant structural collapse is observed, indicating that the M/rGO scaffold provides effective support for the loading and growth of the EuMOF.

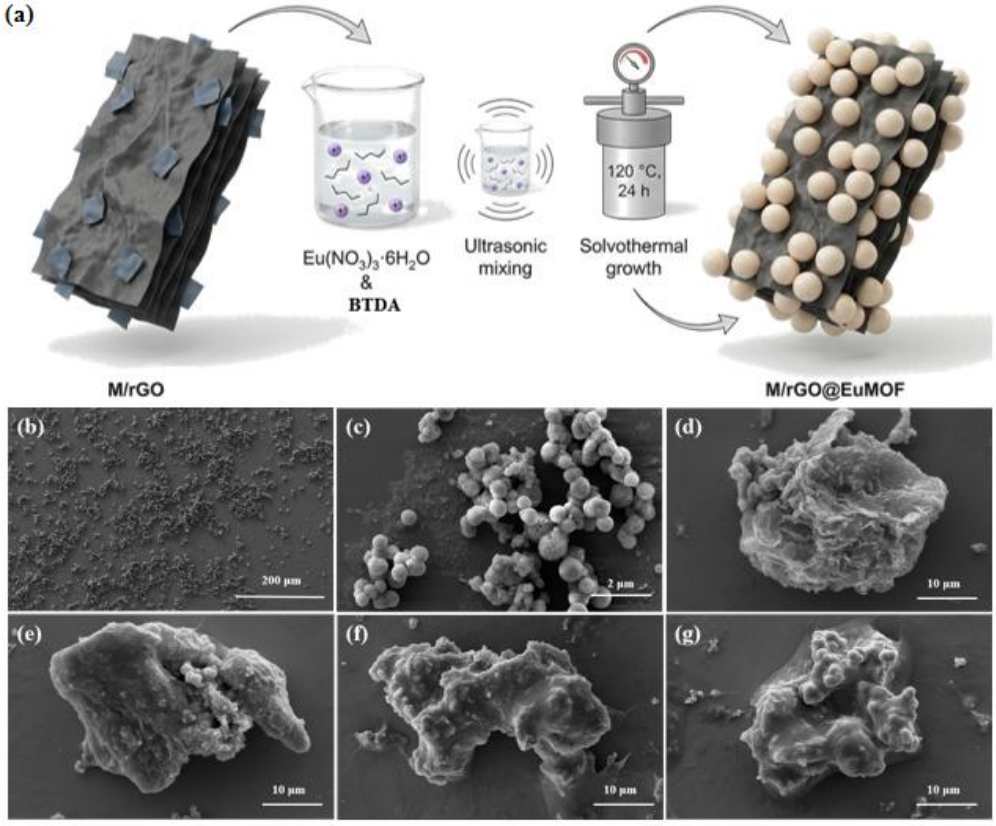

Fig. 1 a Schematic diagram of the preparation process for M/rGO@EuMOF,SEM images: **b,c** EuMOF; **d** MG@E1; **e** MG@E2; **f** MG@E3; **g** MG@E4

3.2 Structural analysis of M/rGO@EuMOF

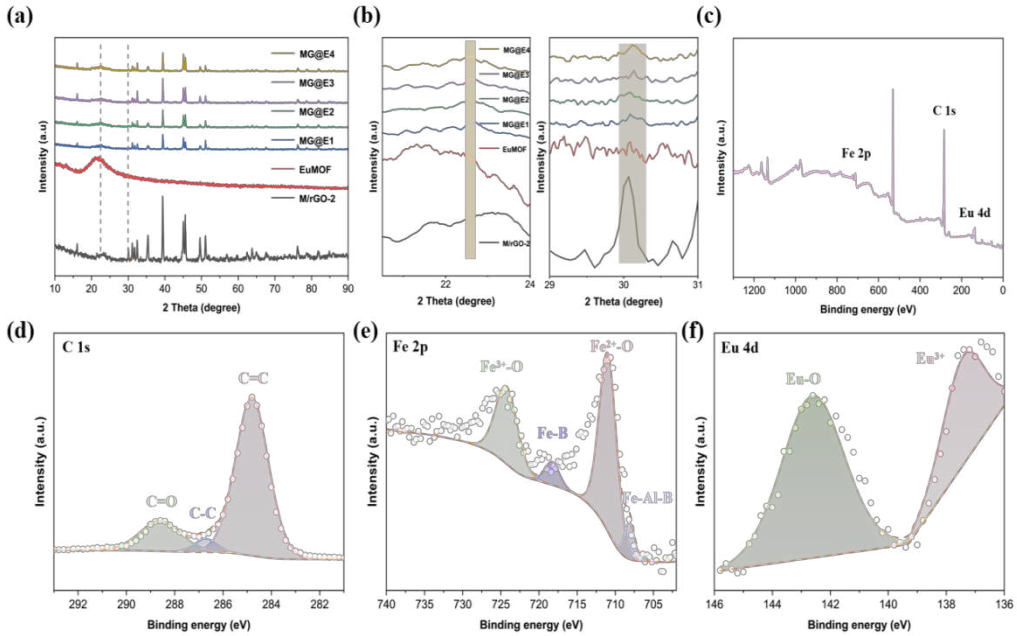

Fig. 2 XRD patterns of **a** M/rGO, **b** EuMOF and **c** M/rGO@EuMOF; XPS spectra of MG@E3: **c** total XPS spectrum, **d** high-resolution C 1s spectrum, **e** high-resolution Fe 2p spectrum; **f** high-resolution Eu 4d spectrum

The crystal structure and surface chemical state of the series of composite materials were characterised using XRD and XPS. As can be seen from the XRD results in Fig. 2a–b, the samples in the MG@E series retained the main diffraction peaks of the M/rGO framework, but the shapes of some peaks underwent significant changes. Near approximately 22°, the characteristic peak originally associated with graphene shifted to the left following the incorporation of EuMOF, overlapping with the characteristic peak of EuMOF in that region and ultimately merging to form a broader diffraction peak. This phenomenon indicates that the introduction of EuMOF alters the stacking state of the graphene layers and the interlayer environment, reflecting strong interfacial interactions between EuMOF and M/rGO, which result in the formation of a heterostructure at the microscopic scale. The characteristic peak near approximately 30° was significantly attenuated following the introduction of EuMOF, indicating that the encapsulation growth of EuMOF weakened the diffraction in this crystal plane direction. This implies that after EuMOF grew on the M/rGO surface, it influenced the local crystal order of the original M/rGO, whilst also indicating that EuMOF had been distributed relatively uniformly across the composite substrate surface. Overall, the introduction of EuMOF did not significantly affect the main skeletal structure of M/rGO, but it did alter the local interlayer structure. Characteristic signals for C, Fe and Eu can be clearly observed in the XPS full spectrum shown in Fig. 2c, confirming that EuMOF has been successfully introduced into the M/rGO system. The high-resolution C 1s spectrum in Fig. 2d can be resolved into components such as C=C, C–C and C=O, with the C=C peak being dominant. This indicates that a relatively intact sp^2 conjugated carbon framework is retained after composite formation, whilst the presence of oxygen-containing functional groups such as C=O suggests that the material surface retains certain active sites, which is

conducive to the anchoring growth of EuMOF on the surface and the formation of heterointerfaces. In the high-resolution Fe 2p spectrum shown in Fig. 2e, components such as Fe–B, Fe–Al–B, Fe^{2+}–O and Fe^{3+}–O can be distinguished. The presence of Fe–B and Fe–Al–B indicates that the Fe–B framework derived from M/rGO was not disrupted during the composite formation process, and the main structure remains stable; whereas the appearance of Fe–O-related peaks suggests a certain degree of oxidation or metal-oxygen coordination on the material surface. The Eu 4d spectrum in Fig. 2f can be fitted to yield peaks associated with Eu–O and Eu^{3+}, suggesting that Eu exists primarily in a coordinated state. This indicates that Eu^{3+} is not simply adsorbed but is loaded onto the composite system via a coordination structure. Taken together, EuMOF has been successfully anchored and incorporated onto the M/rGO surface, forming a stable heterostructure that retains the conductive and magnetic framework of M/rGO whilst effectively incorporating EuMOF [33, 34].

3.3 Absorption Properties and Analysis of M/rGO@EuMOF

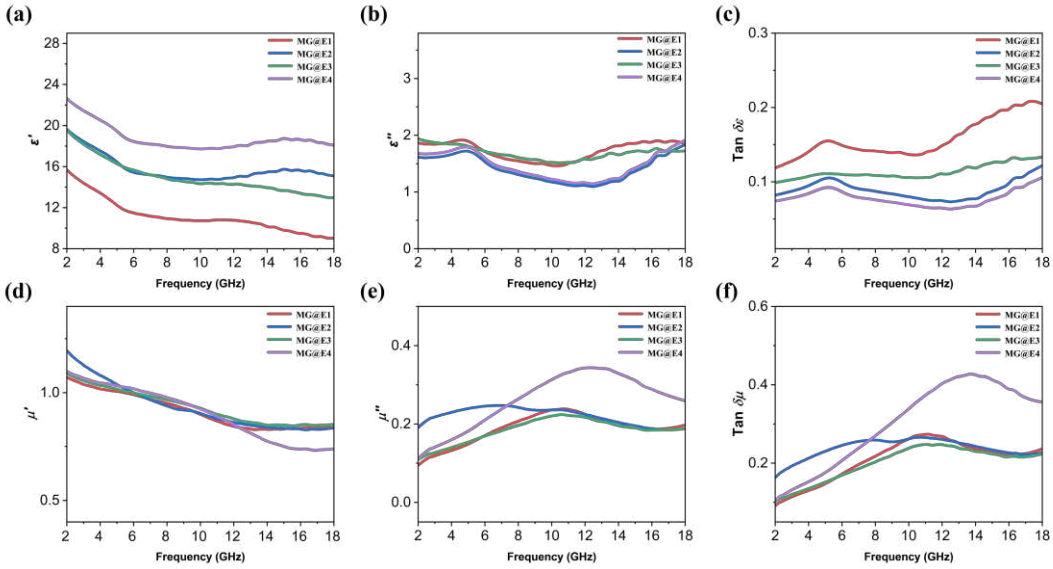

Fig. 3 Electromagnetic parameters of MG@E1, MG@E2, MG@E3 and MG@E4: **a** real part of the dielectric constant, ε′; **b** imaginary part of the dielectric constant, ε"; **c** tangent of the dielectric loss, tan δ; **d** real part of the magnetic permeability, μ′; **e** imaginary part of the magnetic permeability, μ″; **f** tangent of the magnetic permeability, tan δ_μ

The electromagnetic parameters of composite samples with varying EuMOF loadings in the 2–18GHz range were measured using the coaxial method; the results are shown in **Fig. 3.** MG@E1 exhibits a relatively low overall ε′, whereas MG@E2, MG@E3 and, in particular, MG@E4 display higher ε′ values in the low-frequency region, indicating that the incorporation of EuMOF alters the conductive network. This change in dielectric properties may be attributed to the presence of polar carboxyl ligands and coordinated water molecules within the EuMOF crystals, which induce dipole polarisation relaxation under alternating electromagnetic fields. Concurrently, the EuMOF forms

a rich heterogeneous interface with M/rGO; the accumulated charge at this interface generates interfacial polarisation under the influence of the electric field [35,36]. Furthermore, the intercalation and barrier effects of the spherical MOF particles on the rGO conductive network modulate the intensity of conductive loss [37]. As can be seen from **Fig. 3c**, MG@E1 exhibits the highest tan δ value, indicating that the introduction of an appropriate amount of EuMOF can modulate the original conductive network. For MG@E2 to MG@E4, although ε′ is significantly improved, tan δ does not continue to increase in tandem; this suggests that as the EuMOF content continues to rise, whilst the system's dielectric energy storage capacity is enhanced, the magnitude of dielectric loss does not increase significantly. The real part of magnetic permeability (μ′), the imaginary part (μ''), and the tangent of magnetic permeability (tan δμ) were also measured for the different systems. Following the introduction of high EuMOF content, μ′ decreased overall; this is likely due to the intercalation of micrometre-sized microspheres between the rGO and MBene layers, which increased the spacing between magnetic particles and weakened the magnetic response capability. MG@E4 exhibits relatively high μ′ and tan δμ in the high-frequency range, indicating that at higher EuMOF contents, the composite structure helps to optimise high-frequency magnetic loss behaviour. In **Fig. 3f**, all samples exhibit a broad tan δμ peak near the mid-frequency range, suggesting that magnetic resonance loss remains a significant attenuation mechanism within this frequency band. A comprehensive comparison of **Fig. 3c** and **Fig. 3f** reveals that with increasing EuMOF loading, the magnetic loss advantage of the MG@E series samples gradually diminishes, and the dielectric–magnetic loss mechanisms tend towards equilibrium.

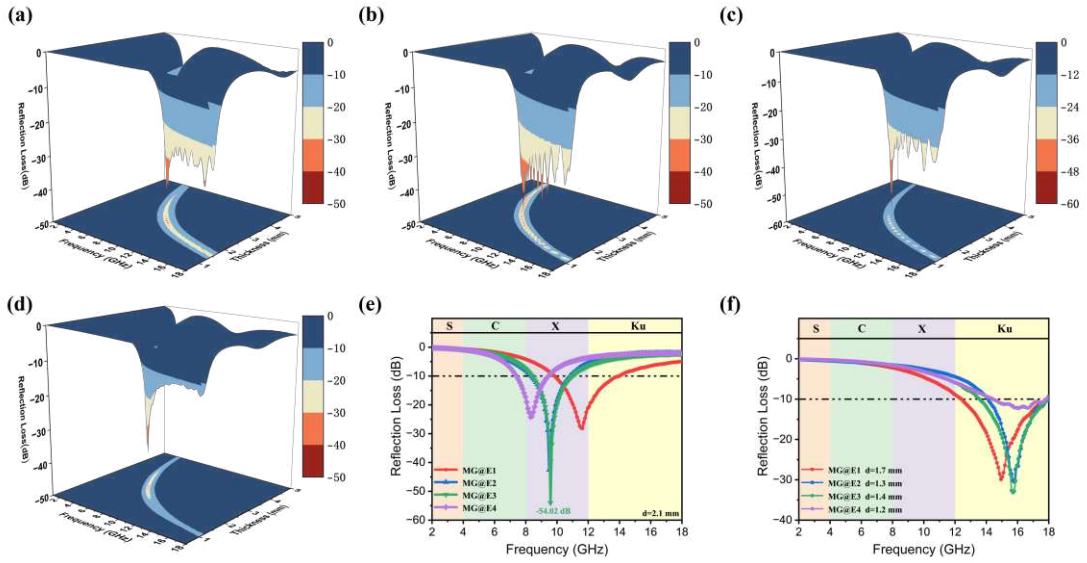

Fig. 4 Three-dimensional RL plots for different samples: **a** MG@E1; **b** MG@E2; **c** MG@E3; **d** MG@E4; **e** Two-dimensional RL plot for a sample with a thickness of 2.1 mm; **f** Widest absorption band width and corresponding widths for different samples

Three-dimensional reflection loss (RL) maps were generated from transmission line theory to visualize the microwave absorption performance of the composites over the 2–18GHz frequency range (Fig. 4). With the

incorporation of EuMOF, the RL distributions evolve markedly, indicating a substantial modulation of the electromagnetic attenuation behavior. For the MG@E1 sample, its minimum reflection loss (RLmin) reaches −41.24dB, and an effective absorption bandwidth (EAB) of 5.4GHz is obtained at a thickness of 1.7mm. When the EuMOF content is increased to that of MG@E2, the RLmin of the sample is enhanced to −46.6dB, indicating that the introduction of EuMOF optimizes the microwave absorption performance of the material to a certain extent. MG@E3 exhibits the optimal comprehensive regulation effect, with an RLmin of −54.02dB and an EAB of 4.5GHz achieved at a thickness of 1.4mm. This demonstrates that a relatively ideal heterogeneous coupling structure is formed between EuMOF particles and M/rGO nanosheets at this loading amount, which increases the number of heterogeneous interfaces and polarization centers and strengthens the interfacial polarization relaxation [38]. However, when the EuMOF content is further increased to that of MG@E4, the microwave absorption performance deteriorates significantly: its RLmin rises to −39.2dB, and the maximum EAB is reduced to 3.9GHz. Both the overall absorption intensity and broadband characteristics are weakened, which is mainly attributed to the fact that excessive EuMOF aggregates on the substrate surface and impairs the continuity of the original conductive network. This conclusion is also supported by the decrease in the conductivity of the system observed from the imaginary part of the permittivity.

The two-dimensional RL curves of the composite samples with different EuMOF loadings were further investigated. Fig. 4e shows the RL curves at a fixed thickness of d=2.1mm, where there are obvious differences in the absorption peak positions and peak intensities among different samples. With the introduction of EuMOF at different contents, the absorption peaks of each composite sample shift to varying degrees, indicating that the addition of EuMOF changes the dielectric/magnetic responses of the system and the propagation behavior of electromagnetic waves inside the material. Among them, MG@E3 shows the strongest reflection loss at the fixed thickness, with an RLmin of −54.02dB, which is significantly superior to those of MG@E1, MG@E2 and MG@E4.As can be seen from the RL curves corresponding to the widest EAB of each sample in Fig. 4f, the absorption peaks of the MG@E series samples are mainly distributed in the high-frequency region, reflecting their excellent high-frequency absorption characteristics. MG@E3 achieves an EAB of 4.5GHz at a thickness of 1.4mm. Combined with Fig. 4e and Fig. 4f, it can be seen that its overall performance is the most outstanding, further confirming that an ideal heterogeneous coupling structure is formed between EuMOF and M/rGO at this loading amount. The widest EAB of MG@E4 is only 3.9GHz, indicating that excessive EuMOF will significantly impair the overall microwave absorption performance.

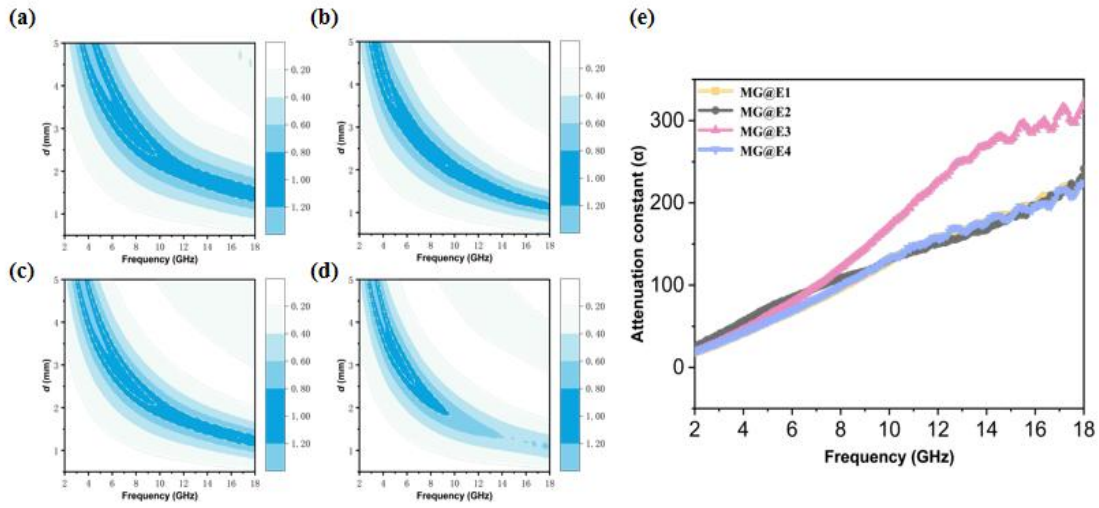

Fig. 5 Impedance matching plots for **a** MG@E1; **b** MG@E2; **c** MG@E3; and **d** MG@E4; **e** Damping constants for different samples

An in-depth analysis of the MG@E series of composites was conducted using normalised impedance matching (|Zin/Z0|) and the attenuation constant α. Typically, Z values within the range of 0.8–1.2(the dark blue region in the figure) indicate good impedance matching characteristics. As can be seen from the two-dimensional impedance matching maps in Fig. 5a–d, the impedance matching of MG@E1 to MG@E3 has been significantly optimised, with the area of the dark blue region markedly expanded and more continuous. This indicates that the addition of an appropriate amount of EuMOF effectively regulates the balance between the complex permittivity and complex permeability, improving the impedance matching between the material and free space, thereby allowing more incident electromagnetic waves to penetrate smoothly into the material. However, when the EuMOF loading was further increased to MG@E4, the dark blue region contracted and narrowed markedly, indicating that excessive EuMOF coating disrupted the balance of electromagnetic parameters, leading to enhanced surface reflection and a renewed mismatch in impedance. Absorption performance is determined jointly by impedance matching and loss capacity; α intuitively reflects the material's ability to dissipate internal electromagnetic waves. As shown in Fig. 5e, the α values of all samples increase with frequency. The moderately loaded MG@E3 sample, although exhibiting α values at low and medium frequencies similar to those of other samples, achieves the highest α value in the system at high frequencies, with the curve exhibiting distinct fluctuations. This indicates that the abundant heterogeneous interfaces formed by the EuMOF induce strong high-frequency interfacial polarisation relaxation, whilst significantly enhancing multiple scattering and reflection of electromagnetic waves within the material [39].

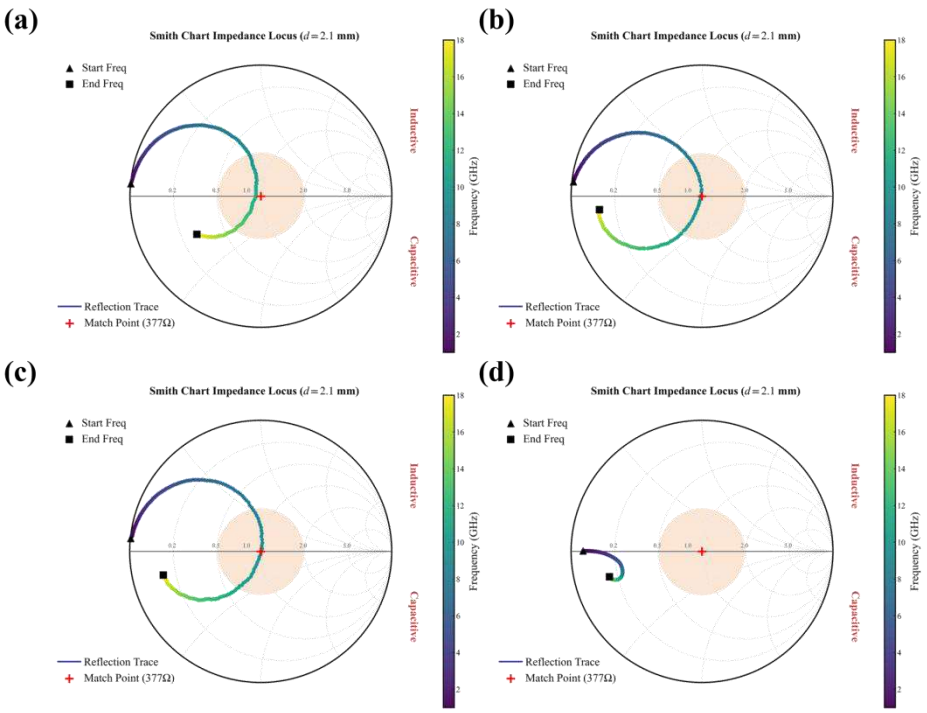

Fig. 6 Smith diagrams for **a** MG@E1; **b** MG@E2; **c** MG@E3; **d** MG@E4

To further investigate the mechanism by which the EuMOF loading regulates the impedance matching characteristics of the composite system, an analysis of the Smith chart impedance trajectories for each sample at a fixed thickness (2.1mm) was conducted, as shown in Fig. 6. The analysis reveals that for the low-loading MG@E1 and MG@E2 samples, their impedance trajectories smoothly enter the light orange matching region as the frequency changes. As the EuMOF content increases moderately, the impedance traces generally show a tendency to converge towards the central matching point. When the EuMOF loading is increased to MG@E3, impedance matching reaches its optimal state: not only does the impedance trace of this sample remain within the high-brightness matching region over a wide frequency range, but the curve also passes through the central red matching marker. This intuitive result is consistent with the two-dimensional impedance matching analysis described earlier. When the EuMOF loading was further increased to an excessive level at MG@E4, the impedance trace on the Smith chart underwent a marked change: the curve not only shortened significantly but also deviated severely towards the left side of the chart, completely falling outside the high-brightness matching region. This extreme deviation indicates that the excessive and densely packed EuMOF particles severely disrupt the balance of the composite material's surface electromagnetic properties. It also confirms the fundamental reason why, as discussed earlier, MG@E4—despite its thin matching layer—exhibits a substantial decline in overall absorption intensity and attenuation constant: electromagnetic waves are extensively reflected at the material's surface and are unable to penetrate into the interior to be dissipated by the loss network.

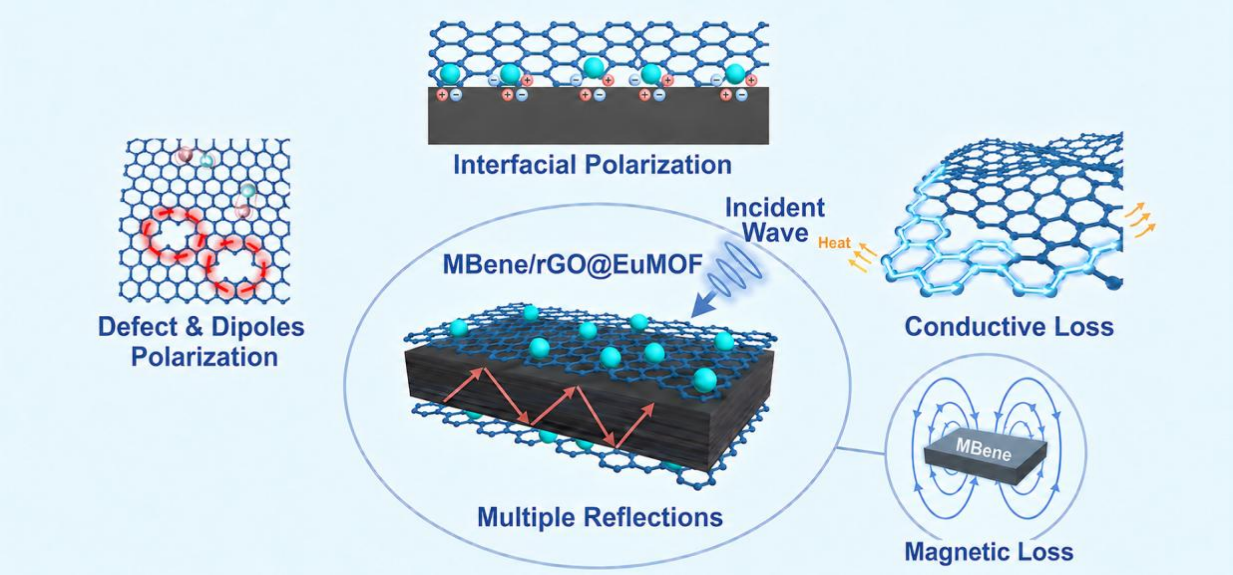

Fig. 7 Schematic illustration of the electromagnetic wave absorption mechanism of MBene/rGO@EuMOF

Based on the above analysis, the microwave absorption mechanism of the MG@E composite is illustrated in Fig. 7. Firstly, EuMOF microspheres uniformly coat the M/rGO surface, forming a zero-dimensional–two-dimensional heterostructure that effectively modulates the system's complex permittivity and complex permeability, thereby significantly improving impedance matching. This allows the majority of incident electromagnetic waves to penetrate into the material, reducing surface reflection. Once inside the material, the continuous three-dimensional conductive network formed by rGO layers and MBene provides a fast pathway for electron migration [40]; simultaneously, the abundant heterogeneous interfaces between EuMOF and M/rGO induce charge accumulation at the interfaces, resulting in strong interfacial polarisation relaxation. Furthermore, the abundant organic ligands, surface residual functional groups and crystal defects within the EuMOF act as dipole polarisation centres, further enhancing dielectric loss under an alternating electromagnetic field [41]. In terms of magnetic loss, the Fe–B magnetic framework exhibits a stable magnetic response across a wide frequency band, effectively facilitating the conversion of electromagnetic waves [42]. Furthermore, the layered crumpled framework and the composite EuMOF jointly establish multiple electromagnetic wave propagation paths, causing the incident wave to undergo multiple reflections and scatter, thereby extending the propagation distance and significantly increasing the probability of energy dissipation.

3.4 Corrosion Protection Properties and Analysis of M/rGO@EuMOF

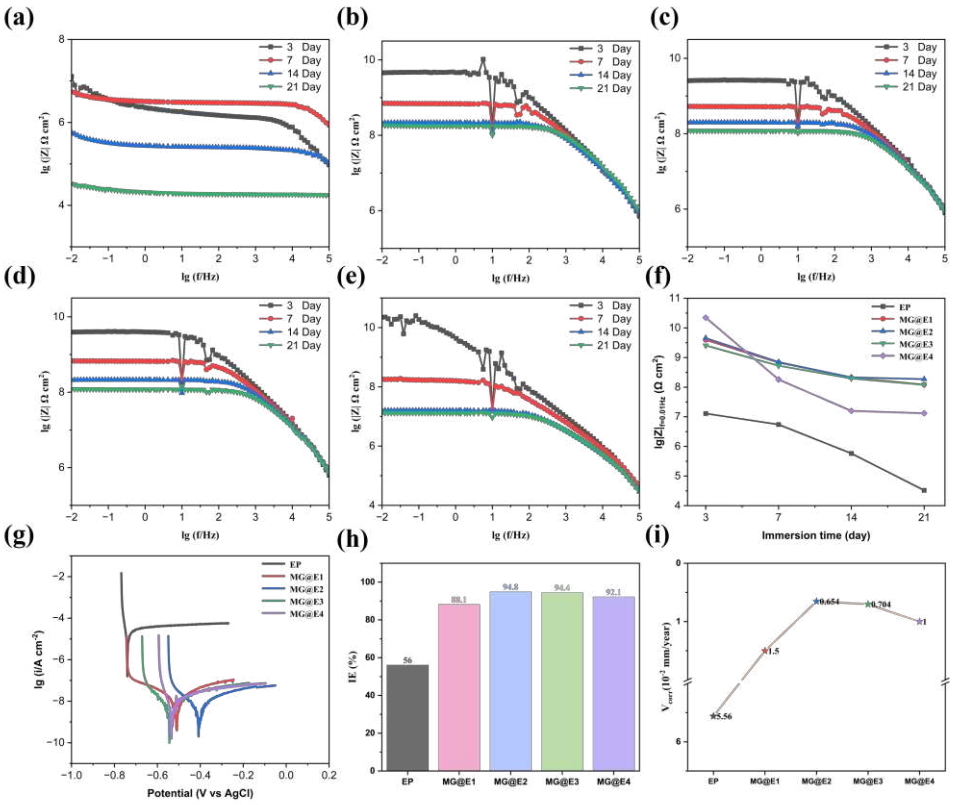

Fig. 8 EIS Nyquist plots of Q235 steel coated with **a** EP, **b** MG@E1, **c** MG@E2, **d** MG@E3, and **e** MG@E4 after immersion in 3.5 wt.% NaCl solution for 3, 7, 14, and 21 days; **f** Variation of lg|Z| at f = 0.01 Hz with immersion time; **g** Tafel curves; **h** Protection efficiency; **i** Annual corrosion rate

The corrosion resistance of the coatings was evaluated by electrochemical impedance spectroscopy (EIS). Fig. 8 shows the changes in impedance modulus of pure EP and MG@E series composite coatings after immersion in 3.5wt.% NaCl solution for 3,7,14 and 21 days, respectively. With the extension of immersion time, water and Cl^- gradually penetrate into the coatings, and the low-frequency impedance modulus of all coatings shows a downward trend. However, the protective ability of the MG@E series samples is significantly superior to that of pure EP.The corrosion resistance of the MG@E series coatings exhibits a regulation law that varies with the EuMOF loading amount. The impedance modulus of MG@E1 after 21 days is $1.20\times10^{8}\Omega\cdot cm^2$, which is 3–4 orders of magnitude higher than that of pure EP ($3.28\times10^{4}\Omega\cdot cm^2$). MG@E2 exhibits the most excellent performance, with $|Z|_{0.01}$Hz of $1.87\times10^{8}\Omega\cdot cm^2$ after 21 days, and the attenuation amplitude of the impedance curve with time is the smallest. This indicates that at this ratio, an appropriate amount of EuMOF microspheres and M/rGO nanosheets achieve the optimal dispersion state and heterogeneous coupling, effectively filling the micropore defects generated during the curing process of epoxy resin and constructing an effective physical barrier for blocking [43,44]. With the further increase of loading amount, the impedance modulus of MG@E3 after 21 days is $1.22\times10^{8}\Omega\cdot cm^2$, and its performance is slightly lower than that of MG@E2, indicating that the increase of loading amount begins to have a subtle effect on the dense barrier performance of the coating. When the EuMOF content is increased to that of MG@E4, the corrosion resistance decreases

significantly, and the impedance modulus drops to $1.32\times10^{7}\Omega\cdot cm^{2}$ after 21 days [45]. This indicates that excessive EuMOF cannot fill the pores, but instead introduces more micro-nano scale defects and voids inside the coating, accelerates the diffusion of corrosive media, and weakens the overall shielding ability.

To further evaluate the corrosion resistance of the composite coatings, potentiodynamic polarization curve tests were performed on each coating sample after immersion in 3.5wt.% NaCl solution for 21 days, and the protection efficiency (IE) of the coatings and the annual corrosion rate were calculated according to the following equations:

$$IE(\%) = \left(1 - \frac{i_{corr}}{i_{corr0}}\right) \times 100\%$$

where icorr0 and icorr are the corrosion current densities of the bare Q235 steel and the coated samples, respectively.

The results are shown in the Fig. 8g that after 21 days of immersion, the potentiodynamic polarization behavior of the MG@E series composite coatings is significantly improved compared with that of pure EP. The polarization curve of EP is located in the high current density region with the lowest corrosion potential, reflecting its extremely fast interfacial charge transfer and the weakest shielding effect. In contrast, the curves of the MG@E series composite coatings all shift significantly towards the low current density direction, and the corrosion potential shifts positively as a whole, indicating that the introduction of MG@E can effectively inhibit the electrochemical corrosion process. Fig. 8h presents the quantitative results of protection efficiency. The protection efficiency of pure EP is only 56%, while that of the MG@E series is all increased to more than 88%, among which MG@E2 reaches the highest 94.8% in this series. The annual corrosion rate results shown in Fig. 8i are consistent with the above trend. The annual corrosion rate of MG@E2 is 0.654×10^{-2}mm/year, exhibiting the optimal protective effect in this series [46].

3.5 RCS simulation analysis of M/rGO@EuMOF

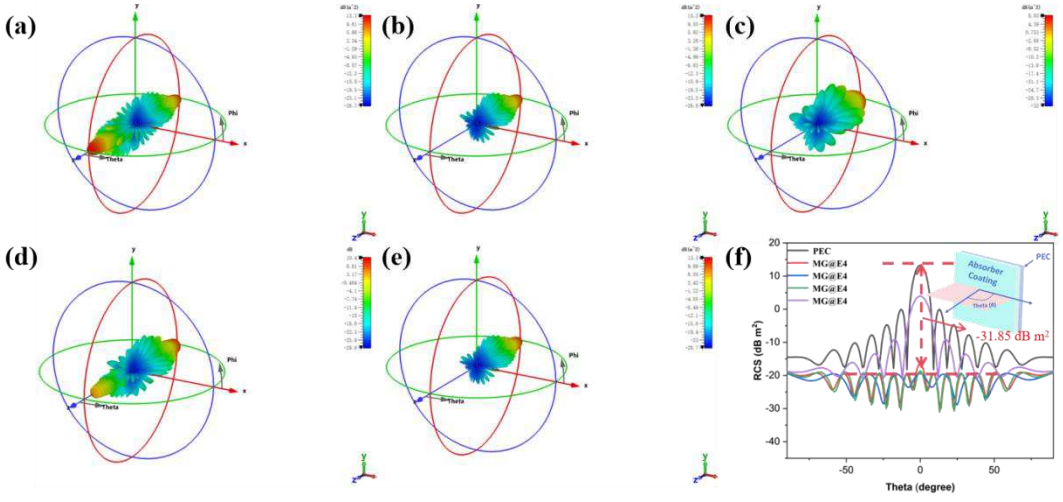

Fig. 9 a PEC, **b** MG@E1, **c** MG@E2, **d** MG@E3, **e** MG@E4: three-dimensional far-field scattering patterns; **f** RCS values as a function of incident angle

To further evaluate the radar stealth capabilities of each sample under far-field conditions, simulation analyses were conducted on the RCS of the PEC and MG@E composite systems [47]. The test conditions were set at a frequency of 9.585GHz, a coating thickness of 2.1mm, and a scanning angle ranging from −90° to 90°; the results are shown in Fig. 9a–f. The three-dimensional far-field scattering patterns clearly demonstrate that the scattering lobe of the PEC is the most prominent, with highly concentrated rearward scattering energy, exhibiting the characteristic of a perfect conductor strongly reflecting incident electromagnetic waves. In contrast, after applying the MG@E1 and MG@E2 absorption layers, the size of the scattering lobe decreased significantly with each step, indicating that the MG@E system is capable of significantly dissipating electromagnetic waves; When the loading was increased to MG@E3, the scattering distribution converged most significantly; the originally concentrated scattering energy was substantially suppressed and dissipated in all directions, with the scattering lobe reaching the smallest size across the entire series, indicating that the material had further optimised the balance between impedance matching and loss capacity at this loading level. However, for the MG@E4 sample, the size of the scattering lobe actually increased markedly compared to MG@E3, with the scattered energy becoming concentrated once again. This is consistent with the previously mentioned analytical conclusion that impedance matching deteriorated, leading to strong reflection of electromagnetic waves at the surface. The curve showing RCS variation with incident angle in Fig. 9f further confirms that, following the addition of the absorption layer, all samples in the MG@E series exhibited a reduction in the 0° peak to varying degrees. Among these, the peak reduction for MG@E3 was the most significant, achieving an RCS attenuation of approximately 31.85dB·m² compared to PEC, demonstrating optimal stealth performance. These simulation results are consistent with the previously mentioned excellent dynamic impedance matching and high-frequency attenuation performance, providing strong evidence of MG@E3's practical application potential in complex electromagnetic environments.

4. Conclusion

In this work, an in-situ growth strategy via the hydrothermal method was adopted to successfully grow EuMOF on the surface of M/rGO, constructing the MG@E series integrated microwave absorption and corrosion protection system. The regulation law of EuMOF loading amount on the microwave absorption and corrosion protection properties of the materials was systematically investigated.In terms of microwave absorption performance, the introduction of an appropriate amount of EuMOF significantly optimized the impedance matching characteristics of the system. The abundant heterogeneous interfaces constructed by EuMOF enhanced the interfacial polarization and dipolar polarization relaxation, which synergized with the conduction loss of rGO and the magnetic loss of MBene. As a result, MG@E3 achieved a minimum reflection loss (RLmin) of −54.02dB at a thickness of 2.1mm and a maximum effective absorption bandwidth (EAB) of 4.5GHz at 1.4mm, exhibiting excellent high-frequency absorption characteristics. RCS simulation further confirmed that MG@E3 could realize a radar cross section (RCS) reduction of 31.85dB·m² at 9.585GHz, demonstrating good far-field stealth capability.In terms of corrosion protection, the performance of MG@E composite coatings was significantly superior to that of pure EP. After immersion in 3.5wt.% NaCl solution for 21 days, MG@E2 still maintained an impedance modulus of $1.87\times10^{8}\Omega\cdot cm^{2}$, with a protection efficiency (IE) of 94.8% and the lowest annual corrosion rate. Its excellent performance originated from the synergistic effect of the "maze effect" of two-dimensional nanosheets and the filling effect of zero-dimensional microspheres.

In summary, MG@E3 achieved well-balanced regulation in terms of microwave absorption intensity, impedance matching, stealth performance and corrosion resistance, providing important experimental basis for the design of multifunctional integrated microwave absorption/corrosion protection materials.

Supporting Information

Suporting Information is available from the Wiley Online Library or from the author.

Acknowledgements

This work was financially supported by National Key Research and Development Program of China (NKRDP, No.2025YFH0100100), the National Natural Science Foundation of China (NSFC, No. 52472305, No. 52302087 and No. 52403049), the Central Funds Guiding Local Science and Technology Development Special Program of Sichuan Province(No. 2025ZYD0156), the Science and Technology Planning Project of Sichuan Province (No. 2026NSFSC1358), and the Fundamental Research Funds for the Central Universities (No.2682025CX057, No.2682026CX022, No.2682026CX197 and No.2682026XJ008) to freely explore basic research projects. In addition, we would like to thank the Analytical and Testing Center of Southwest Jiaotong University for supporting the relative measurements.

Conflict of Interest

The authors declare no conflict of interest.

References

1. X. Xu, D. Li, et al., Architectural design and microstructural engineering of metal–organic framework-derived nanomaterials for electromagnetic wave absorption. Small Struct. 4(1) (2022)
2. J. Liu, S. Tan, et al., A multi-scale cross-band defense system integrating decoupled visible, dynamic infrared camouflage and electromagnetic shielding. Nano-Micro Lett. 18(1), 115 (2026)
3. Z. Fan, S. Li, et al., Magnetic properties, intrinsic ferromagnetic resonance and derived broadband microwave absorption of $BaFe_{12-2x}Ni_xRu_xO_{19}$. J. Phys. Exp. 46(1), 9–16 (2026)
4. Y. Du, X. Zhou, et al., Sub-5 nm high-entropy nanoalloys beyond the Hume-Rothery limit. Nat. Commun. (2026)
5. Z. Zhao, Y. Qing, et al., Advancements in microwave absorption motivated by interdisciplinary research. Adv. Mater. 36(4), e2304182 (2024)
6. W. Wang, D. Liu, et al., Structural design and broadband radar absorbing performance of multi-layer patch using carbon black. Adv. Compos. Hybrid Mater. 5(4), 3137–3145 (2022)
7. P. He, M.J. Zheng, et al., MXene nanohybrids: Excellent electromagnetic properties for absorbing electromagnetic waves. Ceram. Int. 48(2), 1484–1493 (2022)
8. T. Xie, S. Li, et al., Bimetallic MOF-derived composites with broad electromagnetic wave absorption and strong corrosion resistance. Carbon 208, 33–42 (2023)

9. H. Ren, T. Li, et al., Two birds with one stone: Superhelical chiral polypyrrole towards high-performance electromagnetic wave absorption and corrosion protection. Chem. Eng. J. 427 (2022)
10. R. Qin, T. Li, et al., Dielectric-tuned hierarchical nanoarchitectures integrated with volatile corrosion inhibitor systems enable synergistic active-passive anti-corrosion and ultra-broadband microwave absorption. Nano Res. 18(9) (2025)
11. T. Li, Y. Zou, et al., Biomimetic feather-inspired CuHBT superhydrophobic hierarchical architectures for dual-protection excellence in high-performance microwave absorption and corrosion resistance. Small 21(35), e2504567 (2025)
12. R. Li, Z. Liu, et al., Strong metal-support interaction for 2D materials: Application in noble metal/TiB_2 heterointerfaces and their enhanced catalytic performance for formic acid dehydrogenation. Adv. Mater. 33(32), e2101536 (2021)
13. V. Natu, S.S. Kota, et al., X-ray photoelectron spectroscopy of the MAB phases, MoAlB, M_2AlB_2 (M = Cr, Fe), Cr_3AlB_4 and their binary monoborides. J. Eur. Ceram. Soc. 40(2), 305–314 (2020)
14. F.N. Tuzluca Yesilbag, Y.O. Yesilbag, et al., Electrochemical performance of $Fe_2Al_{1-x}B_2$ MBene as a novel electrode material for supercapacitor applications. J. Energy Storage 140 (2025)
15. T. Zhang, B. Zhang, et al., Mo_2B_2 MBene-supported single-atom catalysts as bifunctional HER/OER and OER/ORR electrocatalysts. J. Mater. Chem. A 9(1), 433–441 (2021)
16. J. Pu, S. Fan, et al., F-free fabrication novel 2D Mo-based MBene catalyst for advanced lithium–sulfur batteries. Adv. Funct. Mater. 35(25) (2025)
17. M. Jakubczak, A. Szuplewska, et al., Novel 2D MBenes-Synthesis, structure, and biotechnological potential. Adv. Funct. Mater. 31(38) (2021)
18. B. Lu, G. Jin, et al., Carbon dots intercalated MXene for flexible organic hydrogel absorbers with synergistically enhanced dielectric loss. Nano-Micro Lett. 18(1) (2026)
19. J. Tao, N. Arshad, et al., The quest for two-dimensional MBenes: From structural evolution to solar-driven hybrid systems for water-fuel-energy generation and phototherapy. Small 20(37), e2401603 (2024)
20. M. Jakubczak, D. Bury, et al., Bacterial responses and material-cell interplays with novel MoAlB@MBene. Adv. Healthc. Mater. 14(1), e2402323 (2025)
21. P.A. Yang, L. Wang, et al., Heterogeneous interface engineering and directional tuning electromagnetic parameters of MXene/Fe NPs absorbers for precise low-frequency microwave absorption. Nano Res. 18(11) (2025)
22. J. Mou, S. Li, et al., Deintercalation of Al from MoAlB by molten salt etching to achieve a Mo_2AlB_2 compound and 2D MoB nanosheets. J. Adv. Ceram. 12(5), 943–953 (2023)
23. X. Tan, W. Gu, et al., Carbon-based materials for radar-infrared compatible stealth technology. Chem. Eng. J. 507 (2025)
24. T. Li, J. Li, et al., Top-level electromagnetic design of multishell resonant cavity for microspherical microwave structural absorbers. Small Struct. 6(8) (2025)
25. S. Liu, Y. Lian, Y. Zhao, et al., Recent advances of MXene-based nanocomposites towards microwave absorption: A review. Adv. Compos. Hybrid Mater. 8(1) (2025)

26. G. Zeng, X. Huang, H. Hu, et al., Nanoscale pulverization effect in double-layered MOF-derived hierarchical G/Co@C composites for boosting electromagnetic wave dissipation. Nanoscale 15, 294–303 (2023)
27. Z. Jia, X. Zhang, et al., MOF-derived Ni-Co bimetal/porous carbon composites as electromagnetic wave absorber. Adv. Compos. Hybrid Mater. 6(1) (2022)
28. Z. Zhu, L. Zhang, et al., MOF-derived multicore-shell Fe_3O_4@Fe@C composite: An ultrastrong electromagnetic wave absorber. Carbon 215 (2023)
29. Y. Guo, Y. Duan, et al., Boosting conductive loss and magnetic coupling based on "size modulation engineering" toward lower-frequency microwave absorption. Small 20(17), e2308809 (2024)
30. Y. Zhang, J. Sun, et al., Graphene-like two-dimensional nanosheets-based anticorrosive coatings: A review. J. Mater. Sci. Technol. 129, 139–162 (2022)
31. C. Verma, S. Dubey, et al., Hexagonal boron nitride as a cutting-edge 2D material for additive application in anticorrosive coatings: Recent progress, challenges and opportunities. Mater. Today Commun. 35 (2023)
32. A. Sadanandan, S.A. Thomas, et al., A critical review on two-dimensional $Ti_3C_2T_x$ MXenes for anti-corrosion coatings. Prog. Org. Coat. 183 (2023)
33. C. Petit, T.J. Bandosz, et al., MOF-graphite oxide composites: Combining the uniqueness of metal-organic frameworks and oxide nanosheets. Adv. Mater. 23 (2011)
34. R.H. Li, Z.Q. Liu, Q.T. Trinh, et al., Interfacial engineering of MXene-derived MBene with MOF for electromagnetic wave absorption. Adv. Mater. 33 (2021)
35. L. Yan, Y. Zhang, et al., Utilizing distinctive crystalline/amorphous nano-domains to facilitate multi-polarization behavior for broadband electromagnetic wave absorption. Acta Mater. 294 (2025)
36. Y. Wang, J. Chen, et al., Controllable mesoporous wrinkling design realizes interfacial charge engineering in hierarchical MBene/MoS_2 heterostructures for enhanced microwave absorption. Chem. Eng. J. 169237 (2025)
37. X. Li, Z. Wu, et al., Self-assembly MXene-rGO/CoNi film with massive continuous heterointerfaces and enhanced magnetic coupling for superior microwave absorber. Nano-Micro Lett. 14 (2022)
38. G. Fang, C. Liu, et al., The elaborate design of multi-polarization effect by non-edge defect strategy for ultra-broad microwave absorption. Adv. Funct. Mater. 34 (2024)
39. L. Yan, Y. Zhang, et al., Utilizing distinctive crystalline/amorphous nano-domains to facilitate multi-polarization behavior for broadband electromagnetic wave absorption. Acta Mater. 294 (2025)
40. Z. Ma, K. Yang, D. Li, et al., The electron migration polarization boosting electromagnetic wave absorption based on Ce atoms modulated yolk@shell FexN@NGC. Adv. Mater. 36 (2024)
41. X. Zhang, X. Tian, N. Wu, et al., Metal-organic frameworks with fine-tuned interlayer spacing for microwave absorption. Adv. Sci. 11 (2024)
42. R.H. Li, Z.Q. Liu, Q.T. Trinh, et al., Interfacial engineering of MXene-derived MBene with MOF for electromagnetic wave absorption. Adv. Mater. 33 (2021)
43. X. Lai, J. Hu, et al., Achieving lasting corrosion protection for superhydrophobic epoxy coatings with photothermal conversion property via constructing functionalized graphene nanoplatelet. Carbon 212 (2023)

44. Z. Li, Q. Li, et al., Interfacial engineering of polyaniline/graphene oxide nanosheets with vermiculites for enhancing anticorrosion performance of epoxy coatings. Carbon 248 (2026)
45. W. Sun, Y. Yang, et al., Review on the corrosion-promotion activity of graphene and its inhibition. J. Mater. Sci. Technol. 91 (2021)
46. Y. Zhang, Y. Zhang, et al., Simultaneous enhancement of low-frequency microwave absorption and corrosion resistance in FeSi alloys via magnetic-structural heterojunction engineering. Adv. Funct. Mater. 35 (2025)
47. C. Liu, L. Zhu, et al., A novel elastic dome array structure for precise pressure regulation toward tunable microwave absorption. Acta Mater. 296 (2025)